

Article

B_0 Correction for 3T Amide Proton Transfer (APT) MRI Using a Simplified Two-Pool Lorentzian Model of Symmetric Water and Asymmetric Solutes

Yibing Chen ^{1,†}, Xujian Dang ^{1,†} , Benqi Zhao ², Zhuozhao Zheng ², Xiaowei He ¹ and Xiaolei Song ^{3,*} 

¹ Xi'an Key Laboratory of Radiomics and Intelligent Perception, School of Information Sciences and Technology, Northwest University, Xi'an 710069, China; cyb@stumail.nwu.edu.cn (Y.C.); dangxujian@stumail.nwu.edu.cn (X.D.); hexw@nwu.edu.cn (X.H.)

² Department of Radiology, Beijing Tsinghua Changgung Hospital, Beijing 102218, China; zbqa01279@btch.edu.cn (B.Z.); zzza00509@btch.edu.cn (Z.Z.)

³ Center for Biomedical Imaging Research, Department of Biomedical Engineering, Tsinghua University, Beijing 100084, China

* Correspondence: songxl@tsinghua.edu.cn

† These authors contributed equally to this work.

Abstract: Amide proton transfer (APT)-weighted MRI is a promising molecular imaging technique that has been employed in clinic for detection and grading of brain tumors. MTR_{asym} , the quantification method of APT, is easily influenced by B_0 inhomogeneity and causes artifacts. Current model-free interpolation methods have enabled moderate B_0 correction for middle offsets, but have performed poorly at limbic offsets. To address this shortcoming, we proposed a practical B_0 correction approach that is suitable under time-limited sparse acquisition scenarios and for $B_1 \geq 1 \mu\text{T}$ under 3T. In this study, this approach employed a simplified Lorentzian model containing only two pools of symmetric water and asymmetric solutes, to describe the Z-spectral shape with wide and 'invisible' CEST peaks. The B_0 correction was then performed on the basis of the fitted two-pool Lorentzian lines, instead of using conventional model-free interpolation. The approach was firstly evaluated on densely sampled Z-spectra data by using the spline interpolation of all acquired 16 offsets as the gold standard. When only six offsets were available for B_0 correction, our method outperformed conventional methods. In particular, the errors at limbic offsets were significantly reduced ($n = 8$, $p < 0.01$). Secondly, our method was assessed on the six-offset APT data of nine brain tumor patients. Our MTR_{asym} (3.5 ppm), using the two-pool model, displayed a similar contrast to the vendor-provided B_0 -corrected MTR_{asym} (3.5 ppm). While the vendor failed in correcting B_0 at 4.3 and 2.7 ppm for a large portion of voxels, our method enabled well differentiation of B_0 artifacts from tumors. In conclusion, the proposed approach could alleviate analysis errors caused by B_0 inhomogeneity, which is useful for facilitating the comprehensive metabolic analysis of brain tumors.

Keywords: amide proton transfer (APT) MRI; B_0 inhomogeneity correction; brain tumors; Lorentzian fitting; chemical exchange saturation transfer (CEST) MRI



Citation: Chen, Y.; Dang, X.; Zhao, B.; Zheng, Z.; He, X.; Song, X. B_0 Correction for 3T Amide Proton Transfer (APT) MRI Using a Simplified Two-Pool Lorentzian Model of Symmetric Water and Asymmetric Solutes. *Tomography* **2022**, *8*, 1974–1986. <https://doi.org/10.3390/tomography8040165>

Academic Editor: Emilio Quaia

Received: 4 May 2022

Accepted: 27 July 2022

Published: 1 August 2022

Publisher's Note: MDPI stays neutral with regard to jurisdictional claims in published maps and institutional affiliations.



Copyright: © 2022 by the authors. Licensee MDPI, Basel, Switzerland. This article is an open access article distributed under the terms and conditions of the Creative Commons Attribution (CC BY) license (<https://creativecommons.org/licenses/by/4.0/>).

1. Introduction

As a type of chemical exchange saturation transfer (CEST) imaging [1–3], amide proton transfer (APT) imaging is a promising, non-invasive molecular MRI technique that can detect endogenous mobile proteins and peptides in tissue [4,5]. Numerous institutions worldwide have demonstrated that APT imaging adds important value to the standard clinical MRI sequences in brain tumor diagnoses, such as finding biomarkers, monitoring tumor progression and response to treatment, grading gliomas, etc. [6–9]. Due to the asymmetric nature of CEST signals, asymmetry analysis of the magnetization transfer ratio (i.e., MTR_{asym}) is employed to quantify APT MRI, which equates to the subtraction of

normalized saturation signals at two symmetric offsets around the water frequency (i.e., 0 ppm). MTR_{asym} is susceptible to B_0 inhomogeneity, and B_0 artifacts interfere with the identification and analysis of brain tumors. Therefore, B_0 inhomogeneity correction is important for the quantification and clinical applications of APT imaging.

Limited by the scan time, in the clinical APT protocol, a few saturation offsets are acquired around +3.5 ppm and −3.5 ppm for the post-processing of B_0 inhomogeneity correction, instead of real-time B_0 correction being performed during acquisition [10–13]. The most commonly used post-processing correction methods are interpolation-based methods, which include two steps. First, densely sampled signals with intervals of 0.1 ppm are interpolated from sparsely acquired signals using spline or other interpolated methods [14–18]. Second, the B_0 inhomogeneity is corrected through a B_0 inhomogeneity (ΔB_0) map of the same image geometry. A ΔB_0 map can be obtained using water saturation shift referencing (WASSR) [19,20], Dixon [21], or Lorentzian-based methods [22].

Interpolation-based methods require high-frequency resolutions and signals close to the water frequency to provide line shape and adequate neighborhood information. For example, Debnath et al. found that linear interpolation was suitable for the B_0 correction of APT data ($B_1 = 2 \mu\text{T}$) acquired at 64 offsets (−14~14 ppm with 0.5 ppm intervals) [15]. However, as it is limited by scan time, when using the clinical APT protocol, only a few saturation offsets can be sampled around ± 3.5 ppm. Due to insufficient data acquisition, interpolation-based methods perform poorly at limbic offsets, which means the APT protocol typically only provides MTR_{asym} (3.5 ppm). Therefore, the acquisition signals of the APT protocol are not actually fully used, meaning some important metabolites are discarded, such as the fast exchange amine (2.7 ppm) and semi-solid macromolecules (4.3 ppm) [21].

The a priori introduction of a line-shape constraint may compensate for the disadvantages caused by insufficient data acquisition in the B_0 correction process. Zhou et al. reported Z-spectral line-shapes of brain tumor patients ($B_0 = 3\text{T}$, $B_1 = 2 \mu\text{T}$) in their APT imaging review, which indicates that Z-spectral line-shapes are determined by four effects, i.e., direct water saturation (DS), semi-solid magnetization transfer (MT), CEST and the relayed nuclear Overhauser effect (NOE) [9]. The four effects can be simply divided into two components according to whether the effect is symmetry around water frequency, i.e., a symmetric component including DS, and an asymmetric component including MT, CEST and NOE. Lee et al. proposed a model-based CEST analysis method, which also separated Z-spectra into symmetric and asymmetric parts and used a Lorentzian model to fit the symmetric part [23]. Therefore, limited by few acquisition offsets, a two-pool Lorentzian model may be the correct choice to describe Z-spectral line shapes under 3T with high B_1 , in which one pool fits the symmetric water and another pool fits all asymmetric solutes.

Herein, we propose a practical B_0 correction approach for use in the most popular six-offset acquisition protocol [24]. Using this approach, we employed a two-pool (symmetric water and asymmetric solutes) Lorentzian model to fit the Z-spectral line shape of human brains at 3T with $B_1 = 2 \mu\text{T}$, in a voxel-by-voxel manner. We evaluated our method using in vivo APT data acquired from the brains of healthy volunteers and tumor patients. The contributions of the present study are as follows: (a) In theory, we propose a simplified two-pool Lorentzian model that is suitable to describe the Z-spectral line shape of human brains under 3T with $B_1 \geq 1 \mu\text{T}$. The reduced number of model parameters allowed for fitting using less frequency offsets, i.e., six offsets as in the popular APT protocol. (b) Compared with conventional model-free interpolation, the proposed method could better recover the Z-spectral signals and improve B_0 correction performance, especially for limbic offsets.

2. Theory

To robustly describe the Z-spectral line shape under 3T with high B_1 ($2 \mu\text{T}$), a simplified two-pool Lorentzian model was chosen as an a priori line shape to fit the spline-interpolated initial Z-spectra (ranging $\pm 2.5 \sim \pm 4.5$ ppm). Given the small number of acquired offsets

and the broadening of the peaks, we used the simplest standard to construct our two-pool model, i.e., symmetric water was considered as one pool, and all asymmetric solutes were considered as another pool, which included a large portion of semi-solid macromolecules, a relayed nuclear Overhauser effect (NOE), amides and other metabolites. Equations (1) and (2) present the model function of our two-pool Lorentzian method.

$$\frac{S_{sat}(\Delta\omega)}{S_0} = Z_{base} - \sum_{i=1}^2 L_i(\Delta\omega) \tag{1}$$

$$L_i(\Delta\omega) = \frac{A_i}{1 + (\Delta\omega - \Delta_i)^2 / (0.5W_i)^2} \tag{2}$$

where $i = 1$ (symmetric water), 2 (asymmetric solutes); the parameter Z_{base} is used to correct for a constant signal reduction; L_i represents a Lorentzian line with a central offset (Δ_i), peak full width at half maximum (FWHM, W_i), and peak amplitude (A_i); $S_{sat}(\Delta\omega)/S_0$ is the normalized Z-spectrum. Based on previous studies [25,26] and our experiences, the starting points and boundaries of the fitting parameters are shown in Table 1. The flowchart of the proposed B_0 correction procedure is illustrated in Figure 1.

Table 1. Starting points and boundaries of the 2-pool Lorentzian fitting parameters.

	Δ_1	W_1	A_1	Δ_2	W_2	A_2	Z_{base}
start	0	50	25	-2	50	0.1	0.7
lower	-0.5	0	0	-4	-inf	-inf	-inf
upper	0.5	100	50	4	+inf	+inf	+inf

Note: +inf and -inf represent the positive and negative infinity, respectively.

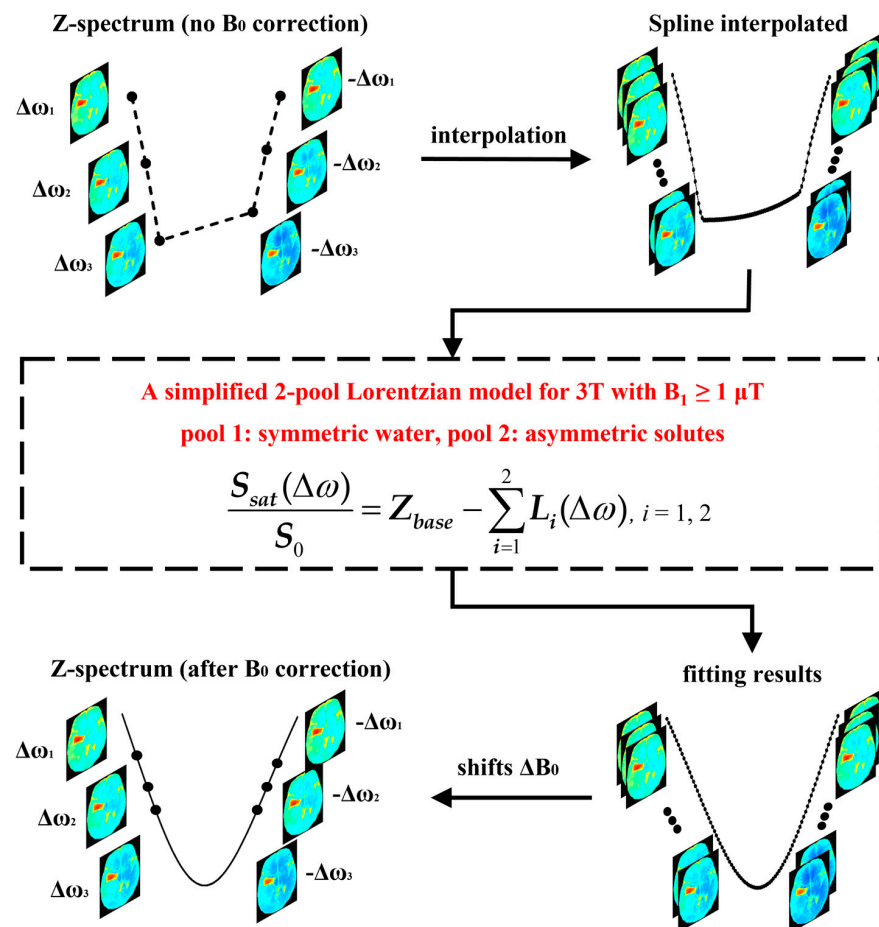


Figure 1. The flowchart of the proposed 2-pool-Lorentzian-based B_0 correction method.

3. Materials and Methods

3.1. B_0 inhomogeneity Correction

The APT data were normalized by S_0 (−1560 ppm) without saturation pulse, and smoothed using a 4×4 median filter according to the acquisition matrix. The proposed 2-pool Lorentzian-based B_0 correction method was used in a voxel-by-voxel manner (Figure 1). For each voxel, a 6-offset Z-spectrum was interpolated, generating a fine Z-spectrum with interval of 0.1 ppm. In this study, the cubic-spline method, implemented by MATLAB 2021, a function spline, was employed for interpolation, because it shows less B_0 artifacts on MTR_{asym} (2.7 ppm) than linear and cubic-Hermite interpolation (Figure S1 in the Supplementary Materials). Then, the 2-pool (i.e., symmetric water and asymmetric solutes) Lorentzian model was utilized to fit the line shape of the interpolated Z-spectrum. Finally, after fitting, the Z-spectrum was shifted along the frequency dimension to the correct position, according to a B_0 inhomogeneity (ΔB_0).

3.2. MTR_{asym} Quantification of APT

After voxel-by-voxel B_0 correction, magnetization transfer ratio asymmetry analysis (i.e., MTR_{asym}) was employed to quantify APT, which is defined as Equation (3).

$$MTR_{asym}(\Delta\omega_j) = \frac{S_{sat}(-\Delta\omega_j) - S_{sat}(\Delta\omega_j)}{S_0} \quad (3)$$

where $\Delta\omega_j$ represents an offset.

3.3. Comparison Methods

The vendor, the cubic-spline interpolation-based method (spline) and the 1-pool Lorentzian-based method (1-pool) were employed as comparison methods. The vendor represents the correction results provided by Philips Healthcare [27]. The 1-pool Lorentzian-based method is similar to the proposed 2-pool Lorentzian-based method, merely replacing the 2-pool (water and solutes) Lorentzian model with the 1-pool (water) Lorentzian model.

3.4. Datasets

In this study, first, we recruited 4 healthy volunteers (2 males and 2 females, aged 22 ± 3.4 years) and 4 brain tumor patients (3 males and 1 female, aged 53.5 ± 14.8 years). From these 8 subjects, densely sampled 16-offset APT data were acquired (−6.7, −5.9, ±5.1, ±4.3, ±3.5, ±2.7, ±1.9, ±1.1 and ±0.3 ppm) to validate the accuracy of our method. Then, we recruited 9 brain tumor patients (3 males and 6 females, aged 54.4 ± 18.6 years), from whom we acquired 6-offset APT data to enable further comparisons with the vendor. Note that the 16-offset APT protocol was modified by us; therefore, it did not include B_0 correction results from the vendor. For our method and comparison methods, 6-offset images (±2.7, ±3.5 and ±4.3 ppm) were extracted from 16-offset APT data. The B_0 correction results using the spline interpolation-based method of 16-offset images were considered to be the gold standard. Of the 13 brain tumor patients, 8 had glioblastomas, 4 had meningiomas and 1 had a metastatic brain tumor from lung cancer.

The study protocol was approved by the institutional review board, and written informed consent was obtained from each subject. MR experiments were performed on a 3T Ingenia MRI system (Philips Healthcare) with a 32-channel phase array coil, using an APT sequence and a turbo spin echo readout. For brain tumor patients, APT data were acquired on the slice centered at the largest areas of the tumors shown on T2w images. The imaging parameters for APT sequences were as follows: $T_{sat} = 2$ s, $B_1 = 2$ μ T, echo time = 8.3 ms, repetition time = 5 s, slice thickness = 7 mm and field-of-view = 220×201 mm² with an acquisition voxel size = $2.5 \times 2.5 \times 7$ mm³. ΔB_0 maps were generated using the 3-echo Dixon. Multi-slice T2w images and Gd-T1w images were acquired with a 5 mm slice thickness.

3.5. Evaluation Metrics

Using the gold standard as described in Section 3.4, Z-spectra errors and MTR_{asym} errors were employed to evaluate the accuracy of B_0 correction, which are defined as Equations (4) and (5).

$$\text{Z-spectra errors} = | \text{Z-spectra}(2\text{-pool/comparisons}) - \text{Z-spectra}(\text{gold standard}) |, \quad (4)$$

$$\text{MTR}_{\text{asym}} \text{ errors} = | \text{MTR}_{\text{asym}}(2\text{-pool/comparisons}) - \text{MTR}_{\text{asym}}(\text{gold standard}) |. \quad (5)$$

One-tailed, paired Student's *t*-tests were used to evaluate the differences between two groups in this study, which were considered to be statistically significant when $p < 0.05$.

4. Results

4.1. Accuracy Evaluation

Figure 2 shows the MTR_{asym} maps and the corresponding error maps of a representative brain tumor patient. As seen in Figure 2a, before B_0 correction, MTR_{asym} maps had severe B_0 artifacts, which would have influenced the identification and analysis of tumors (as shown in Figure 2b), especially for 2.7 ppm. The spline-based correction method alleviated some B_0 artifacts; however, in the regions with high B_0 inhomogeneity ($\Delta B_0 > 0.5$ ppm), the artifacts still appeared on MTR_{asym} (2.7 ppm) and MTR_{asym} (4.3 ppm). The one-pool Lorentzian-based method seemed to eliminate artifacts in regions with high B_0 inhomogeneity, but generated wrong MTR_{asym} (4.3 ppm) maps, which were quite different from the gold standard. Compared with the maps generated using the spline and one-pool methods, the three MTR_{asym} maps corrected using the proposed two-pool Lorentzian-based method not only were more similar to the gold standard, but also had fewer B_0 artifacts. This can also be validated by the MTR_{asym} error maps, shown in Figure 2c. Using our method, there were fewer MTR_{asym} errors of limbic offsets than when using the spline and one-pool methods, especially in the regions with relatively high B_0 inhomogeneity. The MTR_{asym} maps and MTR_{asym} error maps of a representative healthy volunteer are shown in Figure S2 in the Supplementary Materials.

The corresponding region-of-interest (ROI) analyses of the representative tumor patient are shown in Figure 3. Four circle ROIs (radius = 5 voxels) with different B_0 inhomogeneities (ΔB_0) are displayed on T2w and a ΔB_0 map (Figure 3a). As seen in Figure 3b, for the ROIs with relatively low ΔB_0 (~0.1 ppm), i.e., ROI 2 and 3, the line shape of two ROIs were similar to each other, showing almost a direct line from 2.7 to 4.3 ppm and an almost 'invisible' peak at -3.5 ppm. Using the corrected Z-spectra with low ΔB_0 as the internal standard, we found that the Z-spectral line-shape of high ΔB_0 (~0.4 ppm) ROIs, corrected using our method, were similar to the internal standard. In contrast, Z-spectra corrected using the spline showed more obvious peaks at 3.5 ppm. Furthermore, Figure 3c shows that the Z-spectra errors using our method were nearly less than 0.5%, and were also less than those generated using the spline and one-pool methods. Similarly, four ROIs, the mean Z-spectra of ROIs and the corresponding Z-spectra errors of the representative healthy volunteer are shown in Figure S3 in the Supplementary Materials.

We statistically analyzed the Z-spectra errors and MTR_{asym} errors of eight subjects (four healthy volunteers and four brain tumor patients). The results are shown in Figure 4, which were consistent with the experimental results from the representative subject (Figures 2 and 3). As seen in Figure 4a, the spline and one-pool methods performed poorly at the limbic offsets, especially for 4.3 ppm, for which the Z-spectra errors of those two methods were around 1%. In contrast, the Z-spectra error from our method for 4.3 ppm was half of that caused by the spline and one-pool methods (~0.5%). For all the offsets, the Z-spectra errors from our method were the lowest among the three correction methods. From Figure 4b, for all the offsets, the MTR_{asym} errors from our method were less than 0.5% and were significantly lower than those from the spline and one-pool methods ($p < 0.01$). In particular, our method dramatically decreased the MTR_{asym} error of 4.3 ppm.

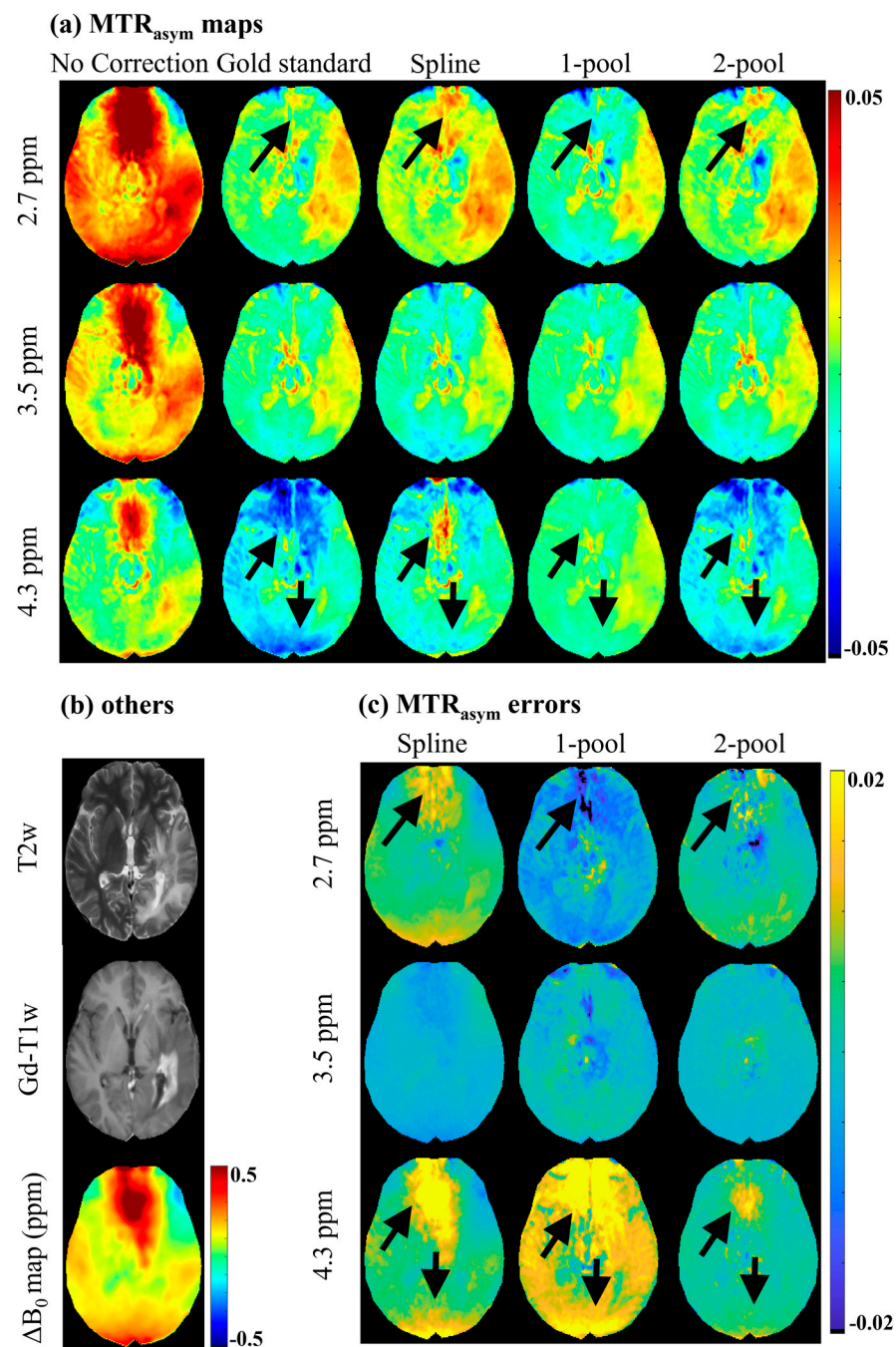


Figure 2. MTR_{asym} maps and MTR_{asym} error maps of a representative brain tumor patient. (a) MTR_{asym} maps without B_0 correction, gold standard, and MTR_{asym} maps corrected using spline, 1-pool Lorentzian and 2-pool Lorentzian methods; (b) T2w, Gd-T1w and ΔB_0 map; (c) the corresponding MTR_{asym} error maps with gold standard.

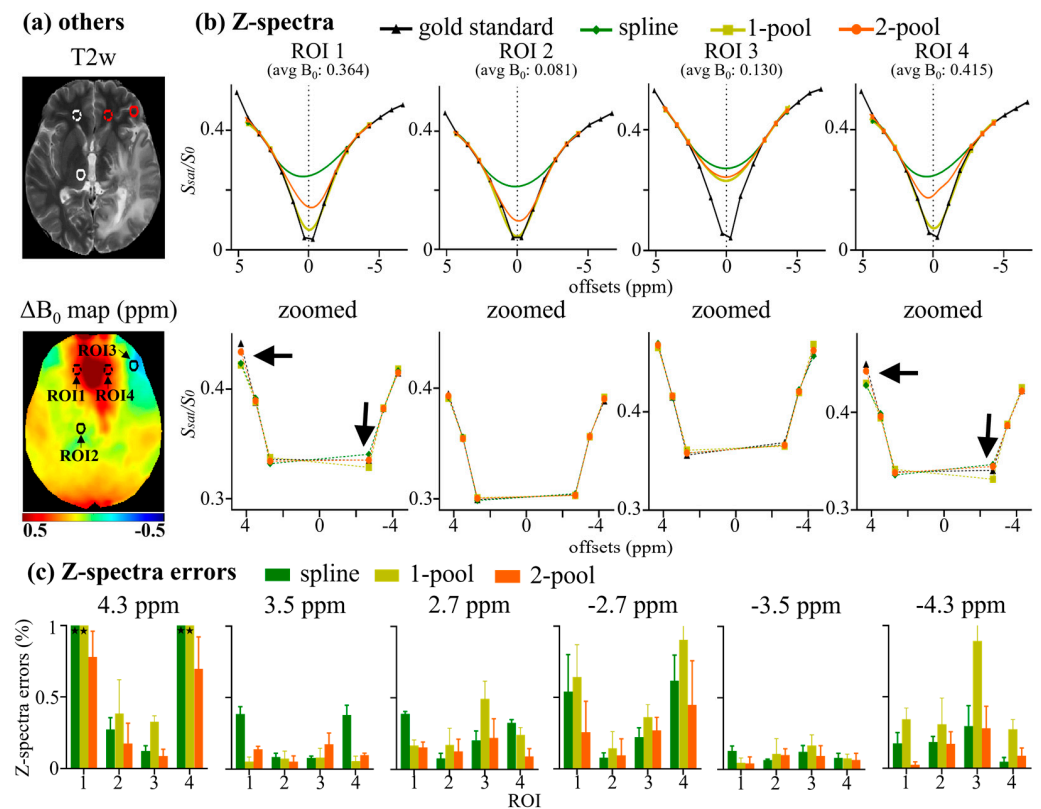


Figure 3. ROI analysis of a representative tumor patient. (a) Four circle ROIs (radius = 5 voxels) with different B_0 inhomogeneity, shown on T2w and ΔB_0 map; (b) mean Z-spectra of ROIs, including gold standard, and Z-spectra corrected using spline, 1-pool Lorentzian, and 2-pool Lorentzian methods; (c) the corresponding Z-spectra error with gold standard.

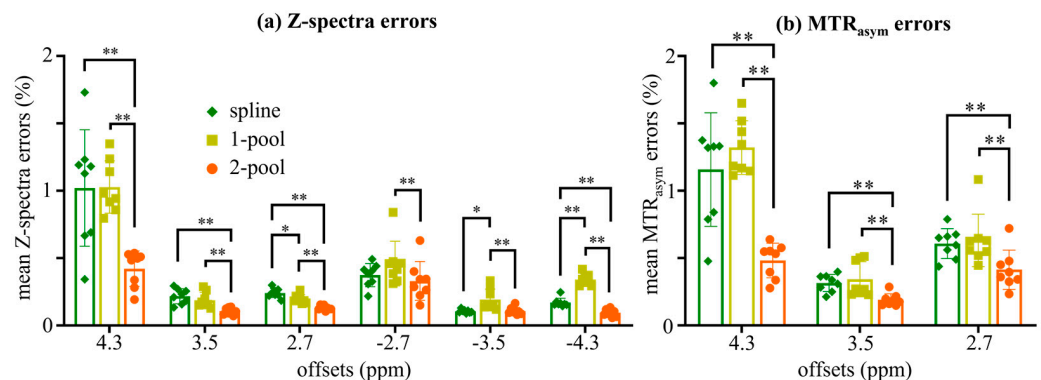


Figure 4. Statistical analysis of 8 subjects (4 healthy volunteers and 4 brain tumor patients). (a) The statistical results of mean Z-spectra errors corrected using spline, 1-pool Lorentzian and 2-pool Lorentzian methods at 6 offsets. (b) The statistical results of mean MTR_{asym} error corrected using spline, 1-pool Lorentzian and 2-pool Lorentzian methods; * $p < 0.05$; ** $p < 0.01$.

As suggested by the experiments with the gold standard, and especially by the statistical results, our method reduced the Z-spectra error and MTR_{asym} error more effectively than the interpolation-based method (i.e., spline) and the one-pool Lorentzian-based method (i.e., one-pool).

4.2. Comparison with Vendor

To compare our method with the vendor, the six-offset APT data of nine brain tumor patients were acquired, as described in Section 3.4. Figure 5 displays the MTR_{asym} maps and corresponding ROI analyses of a representative meningioma patient. Four circle ROIs

(radius = 5 voxels) with different ΔB_0 are shown in T2w, Gd-T1w and a ΔB_0 map (Figure 5a). Figure 5b shows MTR_{asym} without B_0 correction and MTR_{asym} corrected using the vendor, spline, one-pool Lorentzian and two-pool Lorentzian methods. As seen in Figure 5b, the correction results from the vendor still showed obvious B_0 artifacts on MTR_{asym} maps, even for MTR_{asym} (3.5 ppm). Due to the interference of B_0 artifacts, we could not identify the tumor region without Gd-T1w and T2w. The one-pool-Lorentzian-based method also had severe B_0 artifacts, like the vendor. The spline method and our two-pool-Lorentzian-based method efficiently reduced B_0 artifacts, which could help in the identification of tumors. However, the spline-based method still displayed some B_0 artifacts at limbic offsets, especially at 4.3 ppm, while our two-pool-Lorentzian-based method also reduced those artifacts. Similar to the method used in Section 4.1, the corrected Z-spectra of low ΔB_0 ROIs (<0.1 ppm) were considered to be the internal standard for comparison with the corrected Z-spectra of high ΔB_0 ROIs (>0.3 ppm). As seen in Figure 5c, the corrected Z-spectral line shapes observed using our method were close to the internal standard, while the use of the spline method caused a peak at 3.5 ppm, and the line shapes observed using the one-pool method were too symmetric.

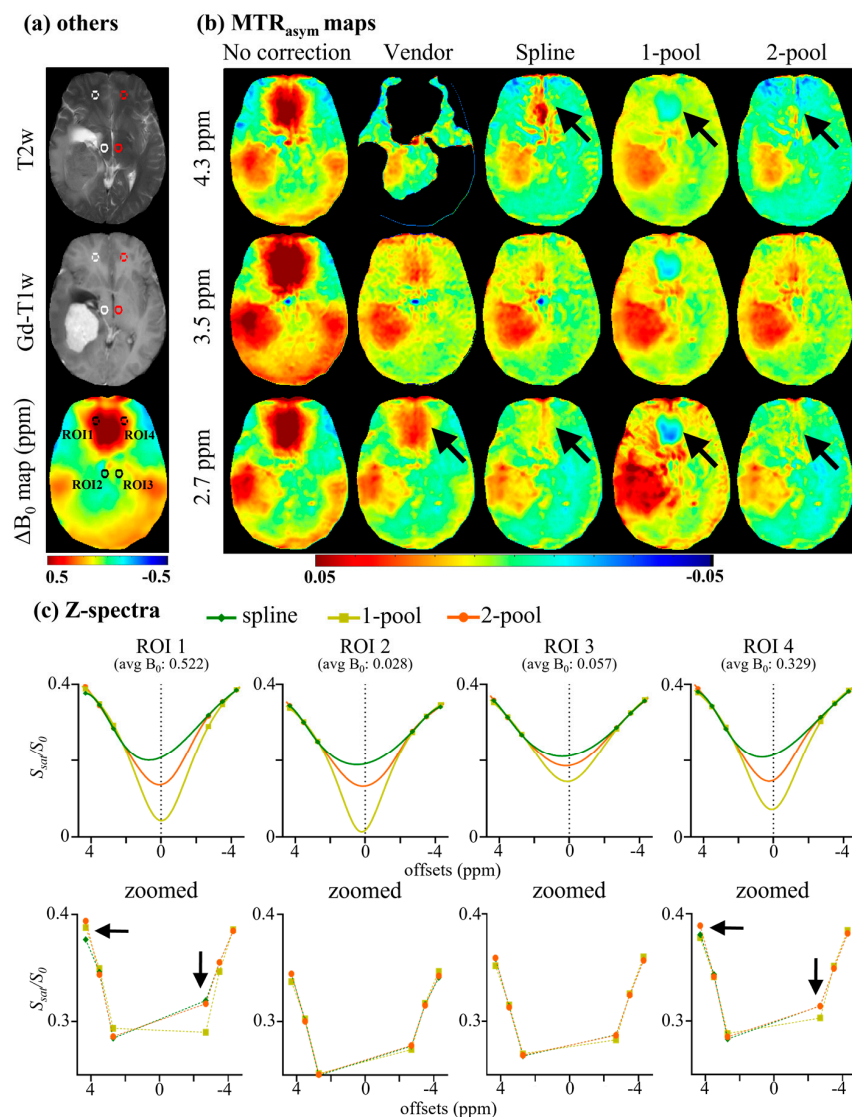


Figure 5. MTR_{asym} maps and ROI analysis of a meningioma patient. (a) Four circle ROIs (radius = 5 voxels) with different B_0 inhomogeneities, shown on T2w, Gd-T1w, and ΔB_0 map; (b) MTR_{asym} maps without B_0 correction and MTR_{asym} maps corrected using vendor, spline, 1-pool Lorentzian and 2-pool Lorentzian methods; (c) mean Z-spectra of ROIs.

To further evaluate the effects of B_0 inhomogeneity on tumor analysis, we compared the mean MTR_{asym} values of tumor ROIs and high ΔB_0 ROIs ($|\Delta B_0| > 0.25$ ppm), corrected using the vendor, spline and two-pool Lorentzian methods. Tumor ROIs were annotated on Gd-T1w by one experienced radiologist, and high ΔB_0 ROIs were generated via threshold segmentation with threshold values = 0.25 ppm. Figure 6a shows the tumor ROI (overlapped on Gd-T1w), high ΔB_0 ROI (overlapped on ΔB_0 map) and T2w of another representative patient. As seen in Figures 5b and 6b, MTR_{asym} (4.3 ppm) corrected using the vendor filtered too many voxels; therefore, we excluded it from the statistical analysis. Figure 6c shows that MTR_{asym} corrected using the vendor could not differentiate tumors from B_0 artifacts, while the spline method and our two-pool Lorentzian method could efficiently reduce B_0 artifacts, which enabled tumors and B_0 artifacts to be distinguished ($p < 0.05$). The mean MTR_{asym} values of high ΔB_0 ROIs corrected using our two-pool Lorentzian method were slightly lower than those obtained using the spline method at 2.7 and 4.3 ppm, which may have been due to the reduced B_0 artifacts, such as the regions indicated by black arrows in Figures 2, 5b and 6b.

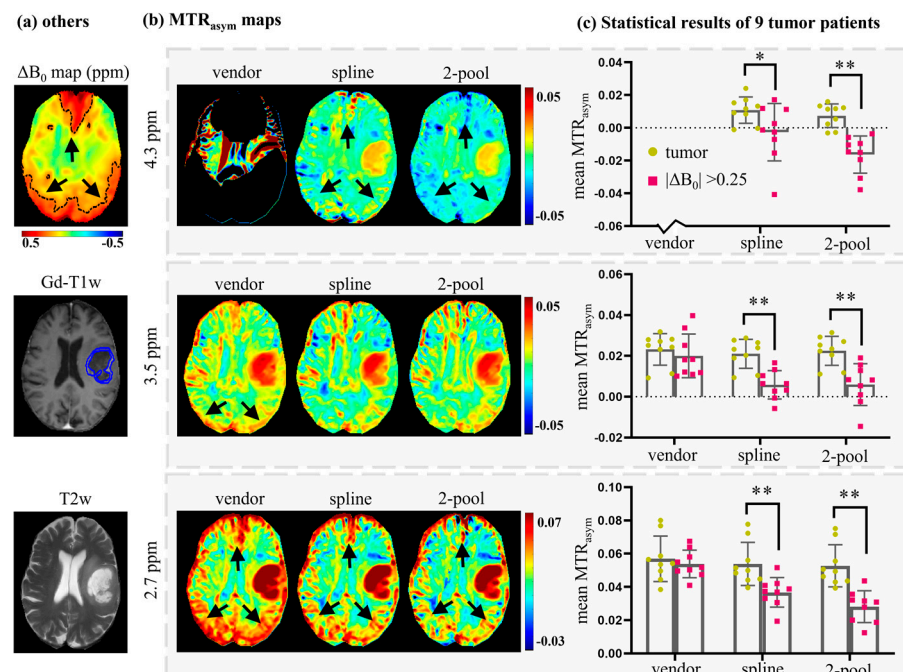


Figure 6. A representative brain tumor patient (a,b) and the statistical results of nine brain tumor patients (c). (a) ROIs of high B_0 inhomogeneity regions (overlapped on ΔB_0 map), ROI of tumor (overlapped on Gd-T1w) and the corresponding T2w. (b) MTR_{asym} maps corrected using the vendor, spline, and 2-pool Lorentzian methods. (c) The statistical results of nine tumor patients, which compared tumor regions with high B_0 inhomogeneity regions on MTR_{asym} corrected using the vendor, spline and 2-pool Lorentzian methods. Because the vendor filtered many voxels of MTR_{asym} (4.3 ppm), we excluded MTR_{asym} (4.3 ppm) provided by the vendor. * $p < 0.05$; ** $p < 0.01$.

5. Discussion

In this study, to improve B_0 correction performance and fully use all the acquisition offsets, we proposed a practical B_0 correction approach for the most popular six-offset acquisition APT protocol. This approach employed a two-pool (symmetric water and asymmetric solutes) Lorentzian line to fit the Z-spectral shape of human brains at 3T with $B_1 = 2 \mu T$, in a voxel-by-voxel manner (Figure 1). We evaluated our method through two kinds of experiments. Firstly, to validate the accuracy of our method, we acquired densely sampled 16-offset APT data of eight subjects, using its spline-interpolation correction results as the gold standard. As suggested by this experiment, and especially by the statistical results, the use of our method reduced MTR_{asym} errors more efficiently than the spline-

interpolation-based method and one-pool-Lorentzian-based method ($p < 0.01$). For 4.3 ppm, the error of Z-spectra and MTR_{asym} corrected using our method were almost half of the errors caused by the spline and one-pool Lorentzian methods (Figures 2–4). Secondly, for comparison with the vendor, we recruited nine brain tumor patients, from whom we acquired six-offset APT data. The experimental results suggested that our two-pool Lorentzian methods efficiently reduced B_0 artifacts, which enabled tumor regions and B_0 artifacts to be distinguished ($p < 0.01$), while the vendor could not differentiate tumors from artifacts (Figures 5 and 6).

Interpolation-based methods are very commonly used in B_0 correction. Debnath et al. compared the B_0 correction performance of different interpolation algorithms with different step sizes on 64-offset APT data ($B_0 = 3T$, $B_1 = 2 \mu T$), and found that linear interpolation-based methods were suitable [15]. As seen in Figure S1, the performance of different interpolation-based methods (linear, cubic-Hermite, and cubic-spline) were similar when using 16 densely sampled offsets. However, for the sparse acquisition scenario (i.e., six offsets), linear and cubic-Hermite showed severe B_0 artifacts on MTR_{asym} (2.7 ppm); cubic-spline (spline) outperformed these two algorithms but still displayed B_0 artifacts. This may suggest that we need to choose interpolation algorithms for B_0 correction with caution when sampled offsets are few, and spline interpolation may be suitable.

The step size of 6-offset APT data is the same with 16-offset data, but 6-offset acquisition does not cover the entire Z-spectrum. Windschuh et al. and Stancanello et al. also indicated that a full Z-spectrum is important for B_0 correction [12,28]. These results may suggest that Z-spectral line shapes are necessary for accurate B_0 correction. Zhou et al. reported that the Z-spectral line shape under 3T with high B_1 is determined via the symmetric effect around water frequency (i.e., direct water saturation) and asymmetric effects (i.e., MT, NOE and CEST) [9,24]. Lee et al. separated Z-spectra into symmetric and asymmetric components for analysis and used a Lorentzian model to fit the symmetric component [23]. In addition, the broadening Z-spectra under 3T with high power did not show specific “visible” peaks. Therefore, a two-pool (symmetric water and asymmetric solutes) Lorentzian model may accurately describe the Z-spectral line shape, which could provide important a priori line-shape information for the B_0 correction of six-offset APT data. As seen in Figure 3, using the Z-spectra of regions with low B_0 inhomogeneity as the internal standard, we found that the Z-spectral line shapes corrected using our method were similar to the internal standard, while those corrected using the spline-based method were determined by acquired data, and those corrected using the one-pool-Lorentzian-based method were too symmetric (Figure 3). The statistical analysis of Z-spectra errors in eight subjects also demonstrated that our method was close to the gold standard and reduced errors more effectively than the spline and one-pool Lorentzian methods (Figure 4).

The proposed method could alleviate the analysis errors caused by B_0 inhomogeneity and could be combined with CEST analysis methods to provide more metabolic information. For example, in this study, we provided more MTR_{asym} maps with higher image quality and less B_0 artifacts than the vendor (Figures 5 and 6), i.e., MTR_{asym} (2.7 ppm) reflecting fast exchange amide, including glutamate and MTR_{asym} (4.3 ppm) reflecting semi-solid MT components. Glutamate is an important energy source for tumor cells, and it always appears in tumor cells that are rapidly growing and dividing [29,30]. In addition, it is a biomarker for the diagnosis and assessment of various psychiatric and neurological disorders [31,32]. MT reflects myelin integrity and, to a lesser extent, cell membrane integrity, which could be used as a biomarker for neurological diseases in which the myelination of the brain is altered, such as in multiple sclerosis [33,34]. Moreover, Mehrabian et al. also found that MT is sensitive to treatment-induced changes in glioblastomas [35].

As the next step, we will combine our method with more CEST analysis methods to provide a comprehensively metabolic delineation of brain tumors. In addition to MTR_{asym} , CEST frequency importance analysis could provide more metabolic features of all the acquired offsets, including upfield NOE offsets [36]. We will also combine our B_0 correc-

tion method with the CEST frequency importance analysis method to fully use all the acquired offsets.

Although our method showed better performance than the interpolation-based method, some limitations remain. (1) In this study, we employed 17 subjects to demonstrate the performance of our method; however, for clinical application, our findings need to be supported by experimental results from studies that have used a larger number of subjects. We will collect more data to evaluate the proposed method more comprehensively. (2) A drawback of the Lorentzian fitting method is the relatively lengthy computation time required. Due to the voxel-by-voxel correction, the computation time of our method was about 7 min for one subject. (3) The Lorentzian fitting method is sensitive to the starting points and boundaries of parameters, and there is not a common method used to determine appropriate starting points and boundaries. Meanwhile, the choice of parameter boundaries influences the fitting time. (4) Limited by the small number of acquisition offsets, we used a simplified two-pool Lorentzian model to replace the multiple-pool model. Fortunately, some studies have focused on accelerating Lorentzian fitting. For example, Yao et al. classified voxels into several clusters, and only conducted Lorentzian fitting once for a cluster to reduce the fitting time [22]. Zaiss et al. employed neural networks to predict the parameters of Lorentzian function, and accelerated Lorentzian fitting to several seconds [37]. In this study, we demonstrated the feasibility of our method. As the next step, we will combine our method, neural networks and densely sampled simulation data, which will enable us to realize a quick multiple-pool Lorentzian-based correction method without tuning fitting parameters.

6. Conclusions

In this study, a practical B_0 -correction approach is proposed, which employed a simplified two-pool Lorentzian model for Z-spectral fitting with $B_1 \geq 1 \mu\text{T}$ under 3T. For both healthy subjects and tumor patients, our approach outperformed conventional interpolation, allowing for better correction at limbic offsets. Therefore, this approach may allow for the efficient extraction of CEST contrast at multiple frequency offsets, and facilitate the more comprehensive metabolic analysis of brain tumors.

Supplementary Materials: The following supporting information can be downloaded at: <https://www.mdpi.com/article/10.3390/tomography8040165/s1>, Figure S1. MTR_{asym} maps corrected employing three interpolation-based methods (i.e., linear, cubic-Hermiter, and cubic-spline), using 16 offsets and 6 offsets, respectively. Figure S2. MTR_{asym} maps and MTR_{asym} error maps of a representative healthy volunteer. (a) MTR_{asym} maps without B_0 correction, gold standard and MTR_{asym} maps corrected using spline, 1-pool Lorentzian and 2-pool Lorentzian methods; (b) T2w, Gd-T1w and ΔB_0 map; (c) the corresponding MTR_{asym} error maps with gold standard. Figure S3. ROI analysis of a representative healthy volunteer. (a) Four circle ROIs (radius = 5 voxels) with different B_0 inhomogeneities, shown on T2w and ΔB_0 map; (b) mean Z-spectra of ROIs, including gold standard, and Z-spectra corrected using spline, 1-pool Lorentzian, and 2-pool Lorentzian methods; (c) the corresponding Z-spectra errors with gold standard.

Author Contributions: Methodology, Y.C., X.D. and X.S.; software, X.D.; formal analysis, Y.C., X.S.; data curation, B.Z., Z.Z.; writing—original draft preparation, Y.C.; writing—review and editing, Y.C., X.D. and X.S.; supervision, X.S., X.H. and Z.Z.; funding acquisition, X.H. and X.S. All authors have read and agreed to the published version of the manuscript.

Funding: This research was funded by the National Natural Science Foundation of China, grant numbers 82071914, 61971350; the National Key R&D Program of China, grant number 2019YFC1521101; the Xi'an Science and Technology Plan, grant numbers 201805060ZD11CG44.

Institutional Review Board Statement: The study was conducted in accordance with the Declaration of Helsinki, and approved by the Institutional Review Board of Beijing Tsinghua Changgung Hospital and school of Medicine, Tsinghua University.

Informed Consent Statement: Written informed consent was obtained from the subjects to publish this paper.

Data Availability Statement: The human data used in this study cannot be shared at this time as the data also form part of an ongoing study.

Acknowledgments: The authors are grateful to Changhao Zhu from Northwest University for his generous help with data processing.

Conflicts of Interest: The authors declare no conflict of interest.

Abbreviations

APT	amide proton transfer
MTR _{asym}	asymmetry analysis of magnetization transfer ratio
CEST	chemical exchange saturation transfer
ΔB_0	B_0 inhomogeneity
WASSR	water saturation shift referencing
DS	direct water saturation
MT	magnetization transfer
NOE	nuclear Overhauser effect
Δ_i	central offset of the Lorentzian line
FWHM	peak full width at half maximum
A_i	peak amplitude
ROI	region-of-interest

References

- Gao, T.; Zou, C.; Li, Y.; Jiang, Z.; Tang, X.; Song, X. A Brief History and Future Prospects of CEST MRI in Clinical Non-Brain Tumor Imaging. *Int. J. Mol. Sci.* **2021**, *22*, 1559. [[CrossRef](#)]
- Okuchi, S.; Hammam, A.; Golay, X.; Kim, M.; Thust, S. Endogenous Chemical Exchange Saturation Transfer MRI for the Diagnosis and Therapy Response Assessment of Brain Tumors: A Systematic Review. *Radiol. Imaging Cancer* **2020**, *2*, e190036. [[CrossRef](#)] [[PubMed](#)]
- Dou, W.; Lin, C.-Y.E.; Ding, H.; Shen, Y.; Dou, C.; Qian, L.; Wen, B.; Wu, B. Chemical exchange saturation transfer magnetic resonance imaging and its main and potential applications in pre-clinical and clinical studies. *Quant. Imaging Med. Surg.* **2019**, *9*, 1747–1766. [[CrossRef](#)]
- Zhou, J.Y.; Payen, J.F.; Wilson, D.A.; Traystman, R.J.; van Zijl, P.C.M. Using the amide proton signals of intracellular proteins and peptides to detect pH effects in MRI. *Nat. Med.* **2003**, *9*, 1085–1090. [[CrossRef](#)] [[PubMed](#)]
- Zhou, J.; Heo, H.-Y.; Knutsson, L.; van Zijl, P.C.M.; Jiang, S. APT-weighted MRI: Techniques, current neuro applications, and challenging issues. *J. Magn. Reson. Imaging* **2019**, *50*, 347–364. [[CrossRef](#)]
- Zhang, J.; Zhu, W.; Tain, R.; Zhou, X.J.; Cai, K. Improved Differentiation of Low-Grade and High-Grade Gliomas and Detection of Tumor Proliferation Using APT Contrast Fitted from Z-Spectrum. *Mol. Imaging Biol.* **2018**, *20*, 623–631. [[CrossRef](#)]
- Jiang, S.; Eberhart, C.G.; Lim, M.; Heo, H.Y.; Zhang, Y.; Blair, L.; Wen, Z.; Holdhoff, M.; Lin, D.; Huang, P.; et al. Identifying Recurrent Malignant Glioma after Treatment Using Amide Proton Transfer-Weighted MR Imaging: A Validation Study with Image-Guided Stereotactic Biopsy. *Clin. Cancer Res.* **2019**, *25*, 552–561. [[CrossRef](#)] [[PubMed](#)]
- Paech, D.; Dreher, C.; Regnery, S.; Meissner, J.E.; Goerke, S.; Windschuh, J.; Oberhollenzer, J.; Schultheiss, M.; Deike-Hofmann, K.; Bickelhaupt, S.; et al. Relaxation-compensated amide proton transfer (APT) MRI signal intensity is associated with survival and progression in high-grade glioma patients. *Eur. Radiol.* **2019**, *29*, 4957–4967. [[CrossRef](#)]
- Zhou, J.; Zaiss, M.; Knutsson, L.; Sun, P.Z.; Ahn, S.S.; Aime, S.; Bachert, P.; Blakeley, J.O.; Cai, K.; Chappell, M.A.; et al. Review and consensus recommendations on clinical APT-weighted imaging approaches at 3T: Application to brain tumors. *Magn. Reson. Med.* **2022**, *88*, 546–574. [[CrossRef](#)]
- Liu, R.; Zhang, H.; Niu, W.; Lai, C.; Ding, Q.; Chen, W.; Liang, S.; Zhou, J.; Wu, D.; Zhang, Y. Improved chemical exchange saturation transfer imaging with real-time frequency drift correction. *Magn. Reson. Med.* **2020**, *83*, 1884. [[CrossRef](#)]
- Simegn, G.L.; Van der Kouwe, A.J.W.; Robertson, F.C.; Meintjes, E.M.; Alhamud, A. Real-time simultaneous shim and motion measurement and correction in glycoCEST MRI using double volumetric navigators (DvNavs). *Magn. Reson. Med.* **2019**, *81*, 2600–2613. [[CrossRef](#)] [[PubMed](#)]
- Windschuh, J.; Zaiss, M.; Ehses, P.; Lee, J.-S.; Jerschow, A.; Regatte, R.R. Assessment of frequency drift on CEST MRI and dynamic correction: Application to gagCEST at 7 T. *Magn. Reson. Med.* **2019**, *81*, 573–582. [[CrossRef](#)] [[PubMed](#)]
- Poblador Rodriguez, E.; Moser, P.; Auno, S.; Eckstein, K.; Dymerska, B.; van der Kouwe, A.; Gruber, S.; Trattig, S.; Bogner, W. Real-time motion and retrospective coil sensitivity correction for CEST using volumetric navigators (vNavs) at 7T. *Magn. Reson. Med.* **2021**, *85*, 1909–1923. [[CrossRef](#)]

14. Yoo, C.H.; Oh, J.; Park, S.; Ryu, C.-W.; Kwon, Y.K.; Jahng, G.-H. Comparative evaluation of the polynomial and spline fitting methods for the B0 correction of CEST MRI data acquired from human brains. *Int. J. Imaging Syst. Technol.* **2019**, *29*, 272–282. [[CrossRef](#)]
15. Debnath, A.; Gupta, R.K.; Reddy, R.; Singh, A. Effect of offset-frequency step size and interpolation methods on chemical exchange saturation transfer MRI computation in human brain. *NMR Biomed.* **2021**, *34*, e4468. [[CrossRef](#)] [[PubMed](#)]
16. Sun, P.Z. Fast correction of B-0 field inhomogeneity for pH-specific magnetization transfer and relaxation normalized amide proton transfer imaging of acute ischemic stroke without Z-spectrum. *Magn. Reson. Med.* **2020**, *83*, 1688–1697. [[CrossRef](#)]
17. Sun, P.Z.; Farrar, C.T.; Sorensen, A.G. Correction for artifacts induced by B-0 and B-1 field inhomogeneities in pH-Sensitive chemical exchange saturation transfer (CEST) Imaging. *Magn. Reson. Med.* **2007**, *58*, 1207–1215. [[CrossRef](#)]
18. Li, Y.; Xie, D.; Cember, A.; Nanga, R.P.R.; Yang, H.; Kumar, D.; Hariharan, H.; Bai, L.; Detre, J.A.; Reddy, R.; et al. Accelerating GluCEST imaging using deep learning for B-0 correction. *Magn. Reson. Med.* **2020**, *84*, 1724–1733. [[CrossRef](#)]
19. Kim, M.; Gillen, J.; Landman, B.A.; Zhou, J.; van Zijl, P.C.M. Water Saturation Shift Referencing (WASSR) for Chemical Exchange Saturation Transfer (CEST) Experiments. *Magn. Reson. Med.* **2009**, *61*, 1441–1450. [[CrossRef](#)]
20. Mueller-Lutz, A.; Matuschke, F.; Schleich, C.; Wickrath, F.; Boos, J.; Schmitt, B.; Wittsack, H.-J. Improvement of water saturation shift referencing by sequence and analysis optimization to enhance chemical exchange saturation transfer imaging. *Magn. Reson. Imaging* **2016**, *34*, 771–778. [[CrossRef](#)]
21. Togao, O.; Keupp, J.; Hiwatashi, A.; Yamashita, K.; Kikuchi, K.; Yoneyama, M.; Honda, H. Amide Proton Transfer Imaging of Brain Tumors Using a Self-Corrected 3D Fast Spin-Echo Dixon Method: Comparison With Separate B-0 Correction. *Magn. Reson. Med.* **2017**, *77*, 2272–2279. [[CrossRef](#)] [[PubMed](#)]
22. Yao, J.; Ruan, D.; Raymond, C.; Liao, L.M.; Salamon, N.; Pope, W.B.; Nghiemphu, P.L.; Lai, A.; Cloughesy, T.F.; Ellingson, B.M. Improving B-0 Correction for pH-Weighted Amine Proton Chemical Exchange Saturation Transfer (CEST) Imaging by Use of k-Means Clustering and Lorentzian Estimation. *Tomography* **2018**, *4*, 123–137. [[CrossRef](#)]
23. Lee, H.; Chung, J.J.; Lee, J.; Kim, S.G.; Han, J.H.; Park, J. Model-Based Chemical Exchange Saturation Transfer MRI for Robust z-Spectrum Analysis. *IEEE Trans. Med. Imaging* **2020**, *39*, 283–293. [[CrossRef](#)]
24. Zhou, J.; Blakeley, J.O.; Hua, J.; Kim, M.; Laterra, J.; Pomper, M.G.; van Zijl, P.C. Practical data acquisition method for human brain tumor amide proton transfer (APT) imaging. *Magn. Reson. Med.* **2008**, *60*, 842–849. [[CrossRef](#)] [[PubMed](#)]
25. Windschuh, J.; Zaiss, M.; Meissner, J.-E.; Paech, D.; Radbruch, A.; Ladd, M.E.; Bachert, P. Correction of B1-inhomogeneities for relaxation-compensated CEST imaging at 7T. *NMR Biomed.* **2015**, *28*, 529–537. [[CrossRef](#)]
26. Cui, J.; Afzal, A.; Zu, Z. Comparative evaluation of polynomial and Lorentzian lineshape-fitted amine CEST imaging in acute ischemic stroke. *Magn. Reson. Med.* **2022**, *87*, 837–849. [[CrossRef](#)] [[PubMed](#)]
27. Van de Ven, K.; Keupp, J. Amide proton transfer weighted imaging: Advancement in molecular tumor diagnosis. *Philips White Pap.* **2018**. Available online: <https://www.documents.philips.com/assets/20180614/1fa1f9ad18a74c2f9388a8ff008b3dcc.pdf> (accessed on 30 June 2022).
28. Stancanello, J.; Terreno, E.; Castelli, D.D.; Cabella, C.; Uggeri, F.; Aime, S. Development and validation of a smoothing-splines-based correction method for improving the analysis of CEST-MR images. *Contrast Media Mol. Imaging* **2008**, *3*, 136–149. [[CrossRef](#)]
29. Goldenberg, J.M.; Pagel, M.D. Assessments of tumor metabolism with CEST MRI. *NMR Biomed.* **2019**, *32*, e3943. [[CrossRef](#)] [[PubMed](#)]
30. Yelamanchi, S.D.; Jayaram, S.; Thomas, J.K.; Gundimeda, S.; Khan, A.A.; Singhal, A.; Keshava Prasad, T.S.; Pandey, A.; Somani, B.L.; Gowda, H. A pathway map of glutamate metabolism. *J. Cell Commun. Signal* **2016**, *10*, 69–75. [[CrossRef](#)]
31. Cui, J.; Zu, Z. Towards the molecular origin of glutamate CEST (GluCEST) imaging in rat brain. *Magn. Reson. Med.* **2020**, *83*, 1405–1417. [[CrossRef](#)]
32. Jia, Y.; Chen, Y.; Geng, K.; Cheng, Y.; Li, Y.; Qiu, J.; Huang, H.; Wang, R.; Zhang, Y.; Wu, R. Glutamate Chemical Exchange Saturation Transfer (GluCEST) Magnetic Resonance Imaging in Pre-clinical and Clinical Applications for Encephalitis. *Front. Neurosci.* **2020**, *14*, 750. [[CrossRef](#)] [[PubMed](#)]
33. Hilbert, T.; Xia, D.; Block, K.T.; Yu, Z.; Lattanzi, R.; Sodickson, D.K.; Kober, T.; Cloos, M.A. Magnetization transfer in magnetic resonance fingerprinting. *Magn. Reson. Med.* **2020**, *84*, 128–141. [[CrossRef](#)] [[PubMed](#)]
34. Mehrabian, H.; Detsky, J.; Soliman, H.; Sahgal, A.; Stanisiz, G.J. Advanced Magnetic Resonance Imaging Techniques in Management of Brain Metastases. *Front. Oncol.* **2019**, *9*, 440. [[CrossRef](#)] [[PubMed](#)]
35. Mehrabian, H.; Myrehaug, S.; Soliman, H.; Sahgal, A.; Stanisiz, G.J. Quantitative Magnetization Transfer in Monitoring Glioblastoma (GBM) Response to Therapy. *Sci. Rep.* **2018**, *8*, 2475. [[CrossRef](#)] [[PubMed](#)]
36. Chen, Y.; Dang, X.; Zhao, B.; Chen, Z.; Zhao, Y.; Zhao, F.; Zheng, Z.; He, X.; Peng, J.; Song, X. Frequency importance analysis for chemical exchange saturation transfer magnetic resonance imaging using permuted random forest. *NMR Biomed.* **2022**, *18*, e4744. [[CrossRef](#)] [[PubMed](#)]
37. Zaiss, M.; Deshmane, A.; Schuppert, M.; Herz, K.; Glang, F.; Ehses, P.; Lindig, T.; Bender, B.; Ernemann, U.; Scheffler, K. DeepCEST: 9.4 T Chemical exchange saturation transfer MRI contrast predicted from 3 T data—A proof of concept study. *Magn. Reson. Med.* **2019**, *81*, 3901–3914. [[CrossRef](#)]